Available online at www.sciencedirect.com
ScienceDirect
Journal of Computational Physics 222 (2007) 644–653
JOURNAL OF COMPUTATIONAL PHYSICS
www.elsevier.com/locate/jcp

A front tracking algorithm for limited mass diffusion ☆

Xinfeng Liu [a], Yuanhua Li [a], J. Glimm [a,b,*], X.L. Li [a]

[a] *Department of Applied Mathematics and Statistics, Stony Brook University, Stony Brook, NY 11794-3600, USA*
[b] *Center for Data Intensive Computing, Brookhaven National Laboratory, Upton, NY 11793-6000, USA*

Received 16 January 2006; received in revised form 3 August 2006; accepted 15 August 2006
Available online 11 October 2006

Abstract

The advantage of front tracking over capturing methods for the numerical simulation of discontinuity surfaces in fluid flow is to eliminate the numerical diffusion of mass across a fluid interface. For accurate modeling of an interface between miscible fluids, however, physical mass diffusion may be significant, and must be added to the calculation. The main purpose of this paper is to introduce a new front tracking algorithm in which the physical diffusion of mass across a tracked interface is included. The accuracy and convergence properties of this algorithm are discussed. The new algorithm is a subgrid algorithm in the sense that the asymptotic fine grid behavior is identical to conventional untracked (capturing) methods while the coarse grid behavior is improved. It is thus most suitable for modeling small values of physical mass diffusion, for which adequate numerical resolution is computationally demanding. The mixing rates for the 3D Rayleigh–Taylor instability of miscible fluids based on this algorithm agree with experimental values.

1. Introduction

The conservation laws

$$\begin{aligned}
&\frac{\partial \rho}{\partial t} + \nabla \cdot \rho \mathbf{v} = \Delta \cdot v\rho, \\
&\frac{\partial \rho \mathbf{v}}{\partial t} + \nabla \cdot \rho \mathbf{v}\mathbf{v} = -\nabla P + \rho g + \nabla \cdot v\mathbf{v}\nabla\rho, \\
&\frac{\partial (\rho E)}{\partial t} + \nabla \cdot ((\rho E + P)\mathbf{v}) = \rho \mathbf{v} \cdot g + \nabla \cdot vE\nabla\rho,
\end{aligned} \tag{1}$$

model the mixing of compressible miscible fluids with physical mass diffusion, where ρ is density, $\mathbf{v}$ is velocity, P is pressure, g is gravity, E is total specific energy, and v is the coefficient of mass diffusion.

☆ Supported in part by the US Department of Energy Grants DE-AC02-98CH10886 and DEFC02-01ER25461, the Army Research office Grant W911NF0510413, and the NSF Grant DMS-0102480.
* Corresponding author. Address: Department of Applied Mathematics and Statistics, Stony Brook University, Stony Brook, NY 11794-3600, USA. Tel.: +1 631 632 8355; fax: +1 631 632 8490.
E-mail address: glimm@ams.sunysb.edu (J. Glimm).

0021-9991/$ - see front matter
doi:10.1016/j.jcp.2006.08.011

The difficulty in solving this system is to eliminate numerical diffusion across an interface between distinct fluids while allowing the correct amount of physical mass diffusion, in the limit where ν is small relative to the affordable grid resolution. The front tracking method [2,3,6,17,18,21] totally eliminates numerical diffusion, but until now it has not allowed the inclusion of small amounts of physical mass diffusion. In this paper, we introduce a new algorithm, building on the front tracking method, to add small amounts of physical mass diffusion while preserving the elimination of numerical mass diffusion across an interface. The improved algorithm is based on the analytical solution of the diffusion equation in one dimension.

Front tracking provides sharp resolution of wave fronts through the active tracking of interfaces between distinct materials. It is a numerical method that represents interfaces explicitly as a lower dimensional mesh moving through a volume filling grid. The time step of the front tracking code *FronTier* consists of two parts, the finite difference interior solver for the states defined on the volume filling rectangular grid and front propagation for the front position and states defined on each side of the front, see [13,3,14,11,16,10]. This propagation of the front points and front state variables distinguishes front tracking from other numerical methods. We use a directionally split method, which breaks the front propagation into normal and tangential steps. For the normal front propagation, we project Eq. (1) to the front normal direction to yield the one dimensional system

$$\begin{aligned}
&\frac{\partial \rho}{\partial t} + \frac{\partial \rho v_N}{\partial N} = \nu \frac{\partial^2 \rho}{\partial N^2},\\
&\frac{\partial \rho v_N}{\partial t} + \frac{\partial (\rho v_N^2 + P)}{\partial N} = \rho g_N + \nu \frac{\partial v_N}{\partial N}\frac{\partial \rho}{\partial N} + \nu v_N \frac{\partial^2 \rho}{\partial N^2},\\
&\frac{\partial \rho v_T}{\partial t} + \frac{\partial \rho v_N v_T}{\partial N} = \nu \frac{\partial v_T}{\partial N}\frac{\partial \rho}{\partial N} + \nu v_T \frac{\partial^2 \rho}{\partial N^2},\\
&\frac{\partial \rho E}{\partial t} + \frac{\partial (\rho E v_N + P v_N)}{\partial N} = \rho g_N v_N + \nu \frac{\partial E}{\partial N}\frac{\partial \rho}{\partial N} + \nu E \frac{\partial^2 \rho}{\partial N^2},
\end{aligned} \tag{2}$$

where $\frac{\partial}{\partial N}$ is the directional derivative in the normal direction $\vec{N}$, $v_N = \mathbf{v}\cdot\vec{N}$, $g_N = g\cdot\vec{N}$, and $v_T = \mathbf{v} - v_N\vec{N}$ is the tangential velocity component (see Fig. 1).

Our primary results are to introduce the new, limited diffusion tracking algorithm, to test this algorithm in 1D examples, and to discuss its extension to 3D. Sample 3D simulation results with experimental validation will be summarized also. In Section 2, the new algorithm to solve the continuity equation with physical diffusion in one dimension is introduced, making use of the front tracking approach. In Section 3, we present computational verification evidence for the proposed algorithm. In Section 4, we extend the algorithm to

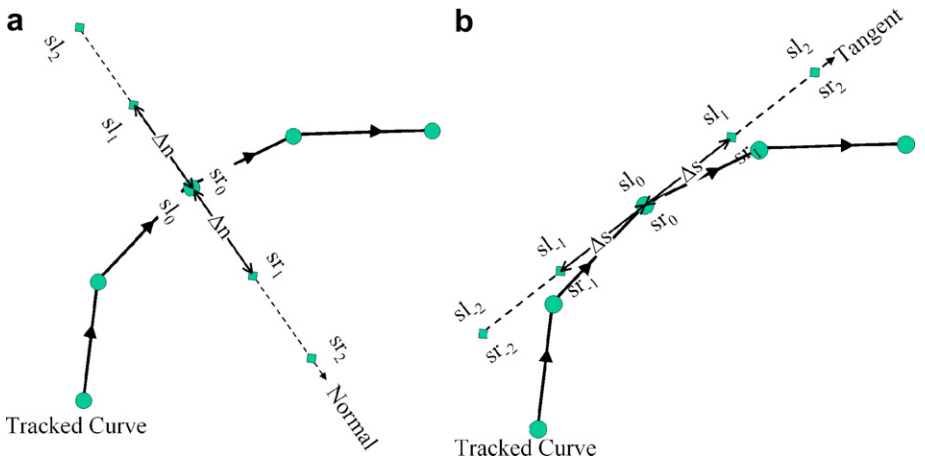

Fig. 1. A schematic showing the normal propagation stencil of states used in propagating a front point. For simplicity the diagram is shown for two spatial dimensions.

higher dimensions. We validate the 3D algorithm by comparing 3D simulations of the Rayleigh–Taylor instability to experimental results.

2. Physical mass diffusion in one dimension

The new algorithm, developed first in 1D, is based on the following ideas. Untracked contact discontinuities give rise to a blurred or smeared out front. We preserve the tracking of a sharp front and introduce physical mass diffusion through it as a perturbation. Thus the time step is split into two parts, the first being the usual non diffusive front tracking [7,12], and the second a pure physical mass diffusion step. Since the first step has been described previously, we only describe the second, physical mass diffusion, step. Conceptually, the front states stored on the tracked front represent the states at $\pm\infty$ relative to the scale of the diffusion layer and the diffusion correction of the interior states near the front will be carried along the characteristics. For the mass diffusion step at each time step, we compare two algorithms. The first is a subgrid algorithm which allows limited mass diffusion according to the analytic form of the solution for the diffusion equation. The second is a finite difference (FD) algorithm. It is conceptually simpler, and computes the desired diffusion across the front based on the interior (nonfront) states, with no regard for any tracked front which might occur within the difference stencil. After the diffusion layer has reached a width of $2\Delta x$, the first algorithm is turned off and replaced with the second. In referring to the finite difference algorithm, we understand the case in which it is used for all times, not just after the diffusion layer width is comparable to the mesh spacing. Both algorithms appear to give satisfactory results, but the subgrid algorithm is superior in computing the amount of mass diffused through the interface. These two algorithms are compared to a finite difference algorithm without tracking.

The subgrid algorithm starts with a reconstruction of the diffusion transition layer. Consider the convection equation with physical diffusion

$$\rho_t + u\rho_x = v\rho_{xx} \tag{3}$$

and the initial condition

$$\rho(x,0) = \begin{cases} \rho_{-\infty} & x < x_0, \\ \rho_{\infty} & x > x_0, \end{cases}$$

where v is the physical diffusion coefficient. This initial value problem can be solved exactly

$$\rho(x,t) = \rho_{-\infty} + \frac{\rho_{\infty} - \rho_{-\infty}}{\sqrt{\pi}} \int_{-\infty}^{(x-X)/\sqrt{4vt}} \mathrm{e}^{-\xi^2}\,\mathrm{d}\xi, \tag{4}$$

where $X = x_0 + ut$.

When Eq. (3) is solved numerically, the finite difference (or finite volume) equation is equivalent to the following modified equation:

$$\rho_t + u\rho_x = (v + \tilde{v})\rho_{xx}, \tag{5}$$

where $\tilde{v}$ is the numerical diffusion. As a result, the numerical solution is approximately

$$\bar{\rho}(x,t) = \rho_{-\infty} + \frac{\rho_{\infty} - \rho_{-\infty}}{\sqrt{\pi}} \int_{-\infty}^{(x-X)/\sqrt{4(v+\tilde{v})t}} \mathrm{e}^{-\xi^2}\,\mathrm{d}\xi. \tag{6}$$

The diffusion widths for the exact solution and numerical solution are $d = \pi\sqrt{vt}$ and $\bar{d} = \pi\sqrt{(v+\tilde{v})t}$ respectively. Since $\tilde{v} \to 0$ as $\Delta x \to 0$, $\bar{d} \to d$ under the mesh refinement.

However, for a large scale computation in three dimensions, mesh refinement is expensive and requires large increases of memory and CPU time. For example, each doubling of the number of grid points in each dimension requires an 8 times increase of memory and a 16 times increase of CPU time. We wish to use finite and affordable computational mesh to simulate realistic physical mass diffusion when the physical diffusion coefficient is substantially smaller than the numerical diffusion coefficient.

Assume that we know the density transition, $\rho^n_{\pm\infty}$, at the current step, the location of the density transition (midpoint), X^n, at the current step, and the amount of mass which has diffused through the interface in either direction up to the current step, $\mathscr{M}^n_\pm$. The density transition and its location are stored as front states and front positions, and updated as part of the (non-diffusive) front and interior state update. The diffused mass, $\mathscr{M}^n_\pm$, is a new variable. It is a diffusion progress variable, and it is updated incrementally within the mass diffusion step. On this basis, we define an analytic solution

$$\rho(x,t^n)=\rho_{-\infty}+\frac{\rho_\infty-\rho_{-\infty}}{\sqrt{\pi}}\int_{-\infty}^{(x-X^n)/\sqrt{4\nu t^n}}\mathrm{e}^{-\xi^2}\,\mathrm{d}\xi. \tag{7}$$

The solution of (7) depends on a time t^n, defined by the property that the integral of $\rho-\rho_{-\infty}$ from $-\infty$ to X^n is just $\mathscr{M}^n_-$.

Thus we define the current (pseudo) time t^n in terms of $\mathscr{M}^n_\pm$ and the current density states at infinity, through the formula

$$\begin{aligned}\mathscr{M}^n_+&=\int_0^\infty(\rho(x,t^n)-\rho^n_{+\infty})\,\mathrm{d}x=(\rho^n_{-\infty}-\rho^n_{+\infty})\int_0^\infty\left(1-\frac{1}{\sqrt{\pi}}\int_{-\infty}^{\frac{x\sqrt{\pi}}{\sqrt{4\pi\nu t^n}}}\mathrm{e}^{-\xi^2}\,\mathrm{d}\xi\right)\mathrm{d}x,\\ \mathscr{M}^n_-&=\int_{-\infty}^0(\rho(x,t^n)-\rho^n_{-\infty})\,\mathrm{d}x=\frac{\rho^n_{+\infty}-\rho^n_{-\infty}}{\sqrt{\pi}}\int_{-\infty}^0\int_{-\infty}^{\frac{x\sqrt{\pi}}{\sqrt{4\pi\nu t^n}}}\mathrm{e}^{-\xi^2}\,\mathrm{d}\xi\,\mathrm{d}x.\end{aligned} \tag{8}$$

Notice $\mathscr{M}^n_-=-\mathscr{M}^n_+$. The increased mass diffused through the middle point at step n is defined as

$$\Delta\mathscr{M}^n_\pm=\mathscr{M}^{n+1}_\pm-\mathscr{M}^n_\pm, \tag{9}$$

where $\mathscr{M}^{n+1}_\pm$ is defined the same as in (8), but with the pseudo time t^n replaced by $t^n+\Delta t$.

As a convention [4], the diffusion layer is reconstructed as a simple piecewise linear curve, defined by a line segment tangent to $\rho(x,t^n)$ through the transition mid point X^n and cutting the horizontal lines $\rho=\rho_{\pm\infty}$. The edges of the reconstructed transition layer are located at $X^n\pm d^n$, where

$$d^n=d(t^n)=\frac{|\rho_\infty-\rho_{-\infty}|}{2|\max_x\rho'(x,t^n)|}\approx\pi\sqrt{\nu t^n}=d^{n-1}\sqrt{1+\frac{\pi^2\nu\Delta t^n}{(d^{n-1})^2}}$$

and the max is computed within the transition zone.

$\mathscr{M}^n_\pm$ is defined incrementally from its previous value by adding the amount of mass to diffuse in the current step. This amount is defined by the analytic solution of (7), using the equivalent time t^n defined in terms of $\mathscr{M}^n_\pm$ and the current time step size Δt. The diffused mass is added to the interior state on one side of the front and subtracted from the interior state on the other.

The subgrid algorithm is applied as long as $d^n<\Delta x$. When $d^n\geqslant\Delta x$ or if the finite difference algorithm rather than the subgrid algorithm is being used, then the diffusion step is a pure centered second order finite difference step, applied to the interior states, with no regard for the front locations, and no use of ghost cells near the front. In either case, the diffusion step defines an amount of mass to be added to or subtracted from that located in the interior states at locations adjacent to the front.

Assume that the velocity and total energy are slowly varying through the transition layer, in comparison to the density variation. On this basis, we also treat the diffusion terms added to the momentum and energy equations as a diffusional correction, and define a parabolic update step for these equations.

To update the interior states, we use operator splitting to separate the hyperbolic from the parabolic terms. A regular stencil is one which does not meet the front. The diffusion term is solved by conventional centered finite differences. For an irregular stencil, if the front cuts a mesh cell not at the center of the stencil, we define ghost cell extrapolation of the states on the same side of the front as the center cell using the front states as in [15]. In case the front cuts the central cell of the stencil, i.e., the cell that the stencil is updating, we use the new algorithm explained below. We denote by $\tilde\rho^{n+1}_i$, $\widetilde{(\rho v)}^{n+1}_i$, $\widetilde{(\rho E)}^{n+1}_i$ the states at x^n_i after the hyperbolic update. Let $\Delta\mathscr{M}^n_\pm$ be defined as above. This mass must be added to the mass described by the interior states. We distribute this increment of diffused mass to the two closest grid cells which lie on each side of the center of the layer. In order to do this, we detect the closest

grid center points on either side of the front center point X_c^{n+1}, namely x_i and x_{i+1}. We add to these cells the mass diffused from the other side

$$\begin{aligned}
\rho_i^{n+1} &= \tilde{\rho}_i^{n+1} + \frac{\Delta\mathscr{M}_-^n}{\Delta x},\\
(\rho v)_i^{n+1} &= (\widetilde{\rho v})_i^{n+1} + \frac{\tilde{v}_i^n \Delta\mathscr{M}_-^n}{\Delta x},\\
(\rho E)_i^{n+1} &= (\widetilde{\rho E})_i^{n+1} + \frac{\widetilde{E}_i^n \Delta\mathscr{M}_-^n}{\Delta x},\\
\rho_{i+1}^{n+1} &= \tilde{\rho}_{i+1}^{n+1} + \frac{\Delta\mathscr{M}_+^n}{\Delta x},\\
(\rho v)_{i+1}^{n+1} &= (\widetilde{\rho v})_{i+1}^{n+1} + \frac{\tilde{v}_{i+1}^n \Delta\mathscr{M}_+^n}{\Delta x},\\
(\rho E)_{i+1}^{n+1} &= (\widetilde{\rho E})_{i+1}^{n+1} + \frac{\widetilde{E}_{i+1}^n \Delta\mathscr{M}_+^n}{\Delta x}.
\end{aligned} \tag{10}$$

3. Validation

First we compare algorithms for a 1D pure diffusion and transport problem in Fig. 2. We set a constant velocity field $v = 0.5$, and study the mass diffusion across a density jump. We compare the exact solution (obtained from a fine grid untracked numerical method) to the subgrid algorithm, the tracked FD algorithm and an untracked FD algorithm. The later three algorithms are computed on a coarse grid, with the final time and the physical values of mass diffusion equivalent to that used in the 3D RT simulation for all figures of Section 3. We choose $v = 0.0008$ in all simulations shown in Section 3. On the scale of three or so mesh blocks, we see that the untracked algorithm is wrong, the tracked FD algorithm is good and the subgrid algorithm is excellent. The excessive mass diffusion in the untracked solution results from the transport within the Euler equation step and not from the computation of diffusion per se.

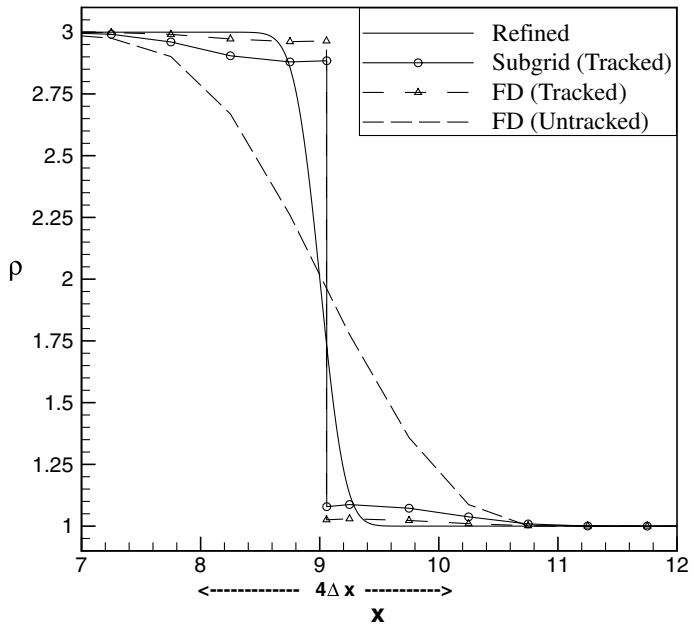

Fig. 2. Comparison of algorithms for the 1D diffusion and transport problem. Plot of density vs time, displayed after 2000 coarse grid time steps and an equivalent physical time for the fine grid.

Fig. 3 compares density contours with different algorithms for the pure transport and diffusion problem, from which we can see that the subgrid (tracked) algorithm is less diffused than the untracked algorithm.

Table 1 compares the L_1 errors for different algorithms for the diffusion and transport problem. We denote by $\rho_{\text{exact}}(x, t^n)$ the exact solution, which can be obtained by a numerical solution using a very fine grid and by $\rho(x, t^n)$ the numerical solution computed on a coarse grid, and interpreted as piecewise linear between grid points. For the two tracked algorithms, the grid cell which contains the front is divided into two fractional cells on either side of the front, and the front states provide the additional data to reconstruct a linear solution in each subcell. We calculate the L_1 error at time t^n by $\int_{-\infty}^{\infty} |\rho(x, t^n)_{\text{exact}} - \rho(x, t^n)| \, dx$.

Table 2 compares the mass diffused through the diffusion layer midpoint X^n at time t^n. For untracked simulations, X^n is defined as the midpoint location of the density within the transition layer. This location is, in general, not a grid point, and so the diffused mass calculation involves use of a fractional cell. The diffused mass is computed by $2\int_{-\infty}^{X^n} |\rho(x, t^n) - \rho_{-\infty}| \, dx$. From this comparison, we see that the subgrid algorithm is far more accurate in this measure of convergence than the FD (tracked and especially untracked) algorithms

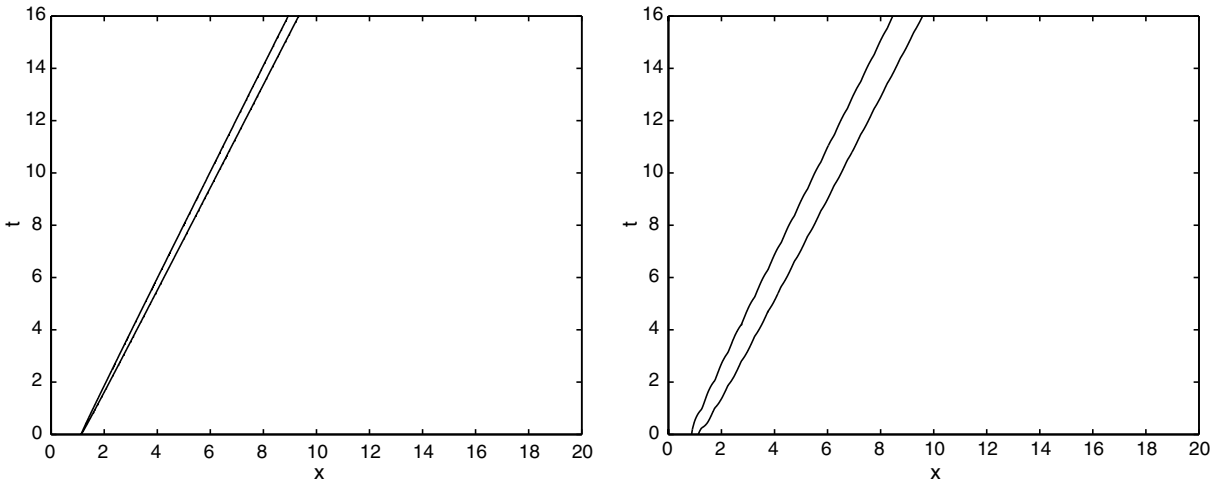

Fig. 3. Comparison of coarse mesh space time density contours for different algorithms. Two contours are shown, for $\rho = 1.5$ and $\rho = 2.5$, that is 25% and 75% of the density change through the transition layer. To avoid stairstep plots of coarse grid piecewise constant functions, we use reconstruction of the transition layer as defined in Section 2. For the untracked FD algorithm, we interpolate data between adjacent grid points. Left: subgrid (tracked) algorithm. The diffusion layer has a width of about $2d^n = 0.8\Delta x$ at time $t = 16$. Right: FD (untracked) algorithm. The numerically computed diffusion layer has a width of about $3\Delta x$ at time $t = 16$.

Table 1
L_1 error comparison for different algorithms

Mesh	Subgrid (tracked)	FD (tracked)	FD (untracked)
40	0.30	0.29	1.02
80	0.28	0.26	0.57
160	0.21	0.20	0.25

Table 2
Comparison of diffused mass for different algorithms at the same time with different grid sizes

Mesh	Subgrid (tracked)	FD (tracked)	FD (untracked)
40	0.240	0.071	1.274
80	0.242	0.129	0.735
160	0.252	0.218	0.480
4000	0.264	0.264	0.264

The coarsest mesh corresponds to the late time 3D simulation.

for a coarse grid, and that the tracked (FD and subgrid) algorithm can eliminate the numerical diffusion across the interface completely. All algorithms agree with a fine grid.

Fig. 4 shows the convergence of the subgrid and the tracked FD algorithms. Both algorithms have good L_1 error norms, even for the coarse grid, with a slight advantage for the FD algorithm.

Fig. 5 compares the algorithms for a shock–contact interaction, again with an imposed velocity field. The left frame is before and the right frame after the interaction of the shock with the contact. The same three algorithms are compared to a fine grid solution. Fig. 6 compares the numerical algorithms before (left) and after (right) a rarefaction wave interacts with the contact interface, parameters chosen as above. From these

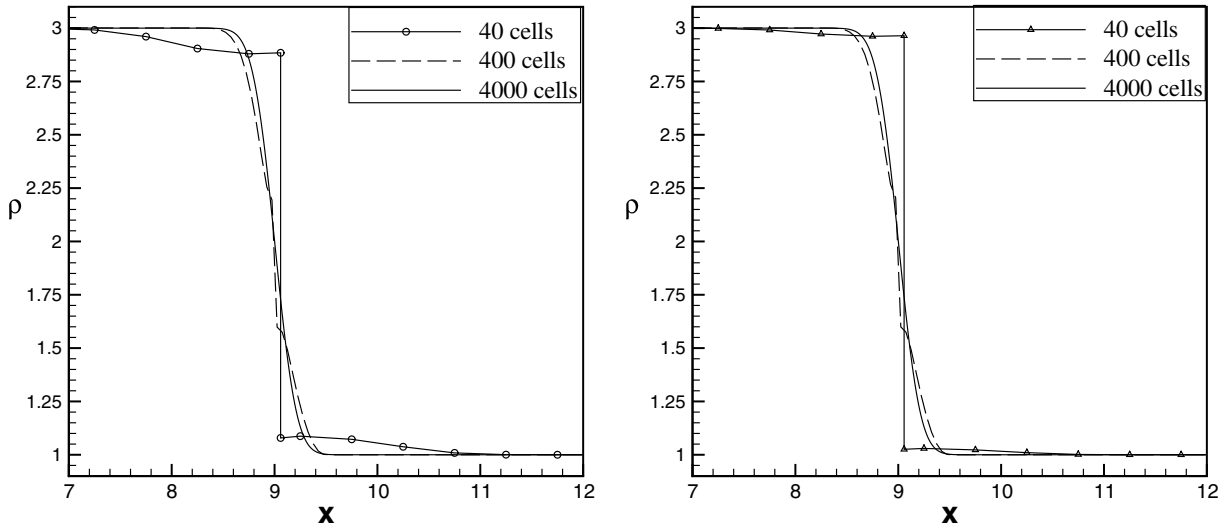

Fig. 4. Convergence of the tracked subgrid and the tracked FD algorithms for the same 1D diffusion and transport problem. Left: the tracked subgrid algorithm; right: the tracked FD algorithm. The coarsest grid coincides with that of Fig. 2.

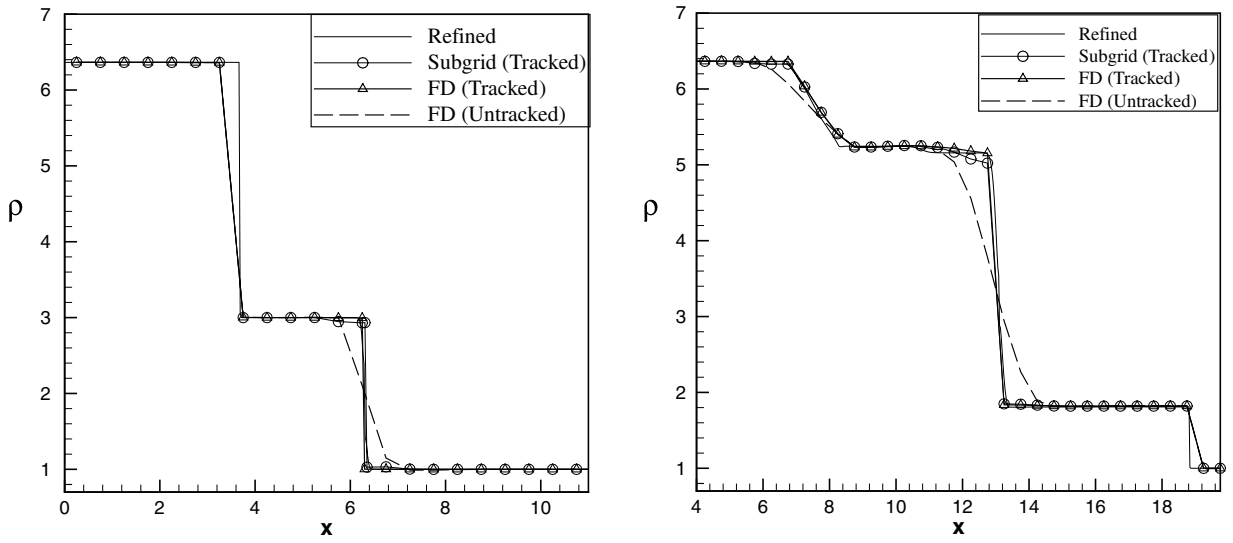

Fig. 5. 1D comparison of algorithms for a shock contact interaction problem. Left: before the shock interacts with the contact; right: after the shock passes through the contact.

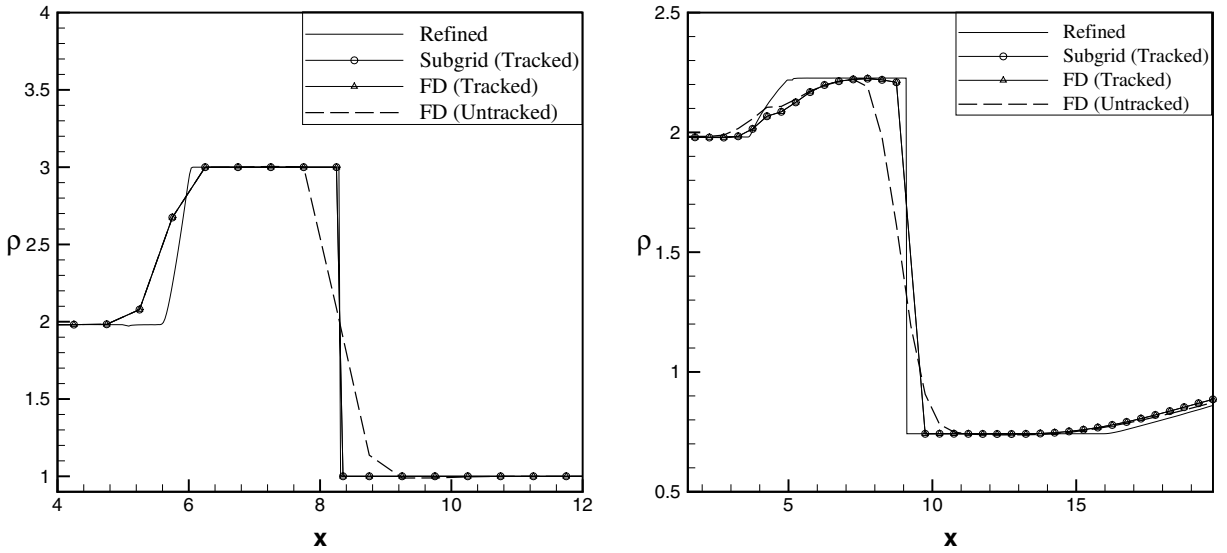

Fig. 6. 1D comparison of algorithms for a rarefaction contact interaction problem. Left: before the rarefaction interacts with the contact; right: after the rarefaction passes through the contact.

three plots, we conclude that the tracked subgrid algorithm and the tracked FD algorithm are nearly equivalent, and both are much better than the completely untracked solution.

4. Extension to higher dimensions

For the higher dimension case, we split the front into normal and tangential directions. The subgrid algorithm is applied along the normal direction, and no diffusion is added to the tangential sweep. In this way, the subgrid algorithm in one dimension can be extended easily and efficiently to the higher dimension. We do not present results from a 3D extension of the tracked FD algorithm, but we remark that it also must be solved in normal-tangential coordinates to avoid over-diffusing the mass. The subgrid algorithm is validated by comparing a 3D simulation of the Rayleigh–Taylor (RT) instability to laboratory experiments [1]. The RT instability occurs at a fluid interface whenever the density gradient is opposed to the acceleration gradient across the interface. The RT mixing rate is the dimensionless coefficient α in the equation

$$h = \alpha A g t^2 \tag{11}$$

for the height h of the bubbles, i.e., the interpenetration distance h of the light fluid into the heavy fluid. Here $A = (\rho_h - \rho_l)/(\rho_h + \rho_l)$ is the Atwood number and t is the time. Acceptable experimental values for α are $\alpha = 0.06 \pm 0.01$ [23,1]. See [22] for background information. To remove effects of mass diffusion (physical and/or numerical), we follow [8] to define a time dependent Atwood number $A(t)$, and the renormalized growth rate α_{ren},

$$\alpha_{\text{ren}} = \frac{h}{2\int_0^t \int_0^s A(r) g \, \mathrm{d}r \, \mathrm{d}s}.$$

Our 3D validation results are summarized in Table 3. See also Fig. 7. Details regarding this simulation will be published separately [20].

5. Discussion

We have introduced a new subgrid algorithm to combine physical mass diffusion with the tracking of an interface (to eliminate numerical mass diffusion between the two fluids). The algorithm has been tested in typ-

Table 3
Mixing rates compared for an air–helium 3D Rayleigh–Taylor experiment and related simulations

Experiment Simulation	Comment	α
Andrews	Miscible [1]	0.07
FronTier	Miscible	0.069
TVD	Untracked [8], ideal	0.035
FronTier	Ideal	0.09
TVD	Untracked, ideal (renormalized)	0.076
FronTier	Miscible, ideal (renormalized)	0.089

The simulations compare physical mass diffusion to ideal physics (no diffusion) and they compare tracked to untracked algorithms. The agreement of the tracked simulation with physical mass diffusion with the experiment is excellent, while the ideal simulations do not agree with experiment, nor (because of the numerical mass diffusion in the untracked ideal simulation) with each other.

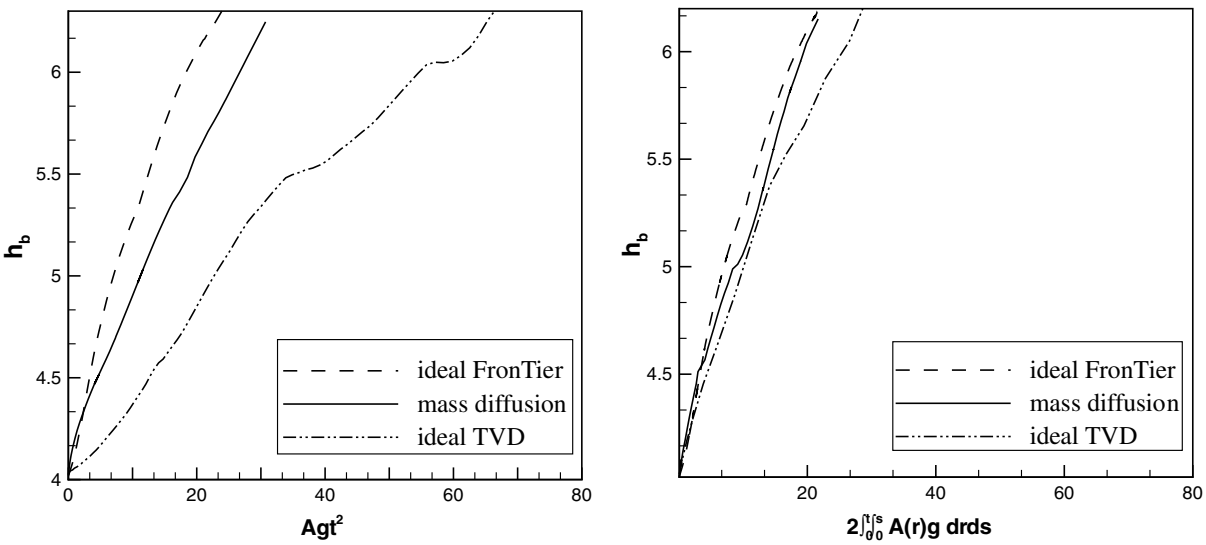

Fig. 7. Left: Self similar growth of the mixing zone. Right: the same data plotted using a time dependent Atwood number, to remove the effects of numerical or physical mass diffusion.

ical 1D wave interaction problems, extended to 3D and then compared to a laboratory experiment of RT mixing rates, with basically perfect agreement. We can also identify two other issues that could contribute opposite effects and at least in part cancel each other, subgrid or unresolved mass diffusion due to unresolved subgrid interfaces and long wave length initial conditions.

Viscosity will be very small for the air–helium experiment but large for other experiments, see the discussion in [20]. The extension of the subgrid algorithm to include the viscosity will definitely be useful and will be our future study.

We omit tangential mass diffusion as this effect is not directly coupled to the diffusion related decrease of buoyancy forces that is activated by the mass diffusion normal to the interface. Similarly we regard curvature related corrections to the diffusion process as secondary. Such phenomena are not considered here but could be studied in following investigations.

This result can be compared to typical untracked simulations, which generally under-predict mixing in comparison to experiment by a factor of 2 [5]. In the study [8], we identified numerical mass diffusion as an explanation of the discrepancy between untracked simulations and experiment.

The total variation diminishing (TVD) algorithm [19] gives a value for the growth rate $\alpha = 0.035$, while for other simulation codes [5], α varies from 0.023 to 0.030. We list three differences between the untracked simulation [19] and the others [5] with the potential to explain these differences: [19] used 2 times the mesh reso-

lution per mode, it used artificial compression to reduce mass diffusion and it used a different numerical algorithm (TVD).

In previous work, we obtained agreement with experimental data for RT mixing of immiscible fluids [9], namely, $\alpha_{\text{numerical}} = 0.067$, $\alpha_{\text{experiment}} = 0.063 \pm 0.013$.

Combining the present study and this previous one, we can state that improved numerical modeling of interfaces (via front tracking) and improved physics modeling (via inclusion of scale breaking phenomena) is an important factor to our agreement between numerical simulation and experiment. We are not aware of other 3D RT mixing simulations with comparable agreement with experiment.

References

[1] A. Banerjee, M.J. Andrews, A gas channel facility to investigate statistically steady Rayleigh–Taylor mixing at high Atwood numbers, Phys. Fluids, in press.
[2] M. Ben-Artzi, The generalized Riemann problem for reactive flow, J. Comput. Phys. 86 (1989) 70–101.
[3] I-L. Chern, J. Glimm, O. McBryan, B. Plohr, S. Yaniv, Front tracking for gas dynamics, J. Comput. Phys. 62 (1986) 83–110.
[4] A. Chorin, J. Marsden, A Mathematical Introduction to Fluid Mechanics, Springer-Verlag, New York, Heidelberg, Berlin, 2000.
[5] G. Dimonte, D.L. Youngs, A. Dimits, S. Weber, M. Marinak, S. Wunsch, C. Garsi, A. Robinson, M. Andrews, P. Ramaprabhu, A.C. Calder, B. Fryxell, J. Bielle, L. Dursi, P. MacNiece, K. Olson, P. Ricker, R. Rosner, F. Timmes, H. Tubo, Y.-N. Young, M. Zingale, A comparative study of the turbulent Rayleigh–Taylor instability using high-resolution three-dimensional numerical simulations: the alpha-group collaboration, Phys. Fluids 16 (2004) 1668–1693.
[6] J. Donea, S. Giuliani, J.P. Halleux, An arbitrary Lagrangian–Eulerian finite element method for transient dynamic fluid–structure interactions, Comput. Methods Appl. Mech. Eng. 33 (1982) 689–723.
[7] Jian Du, Brian Fix, James Glimm, Xicheng Jia, Xiaolin Li, Yunhua Li, Lingling Wu, A simple package for front tracking, J. Comp. Phys. 213 (2006) 613–628, Stony Brook University preprint SUNYSB-AMS-05-02.
[8] E. George, J. Glimm, Self similarity of Rayleigh–Taylor mixing rates, Phys. Fluids 17 (2005) 054101-1–054101-13, Stony Brook University Preprint number SUNYSB-AMS-04-05.
[9] E. George, J. Glimm, X.L. Li, Y.H. Li, X.F. Liu, The influence of scale-breaking phenomena on turbulent mixing rates, Phys. Rev. E 73 (2006) 016304-1–016304-5.
[10] J. Glimm, J.W. Grove, X.L. Li, W. Oh, D.H. Sharp, A critical analysis of Rayleigh–Taylor growth rates, J. Comput. Phys. 169 (2001) 652–677.
[11] J. Glimm, J.W. Grove, X.-L. Li, K.-M. Shyue, Q. Zhang, Y. Zeng, Three dimensional front tracking, SIAM J. Sci. Comput. 19 (1998) 703–727.
[12] J. Glimm, J.W. Grove, X.-L. Li, N. Zhao, Simple front tracking, in: G.-Q. Chen, E. DiBenedetto (Eds.), Contemporary Mathematics, vol. 238, American Mathematical Society, Providence, RI, 1999, pp. 133–149.
[13] J. Glimm, J.W. Grove, Y. Zhang, Interface tracking for axisymmetric flows, SIAM J. SciComp. 24 (2002) 208–236, LANL Report No. LA-UR-01-448.
[14] J. Glimm, E. Isaacson, D. Marchesin, O. McBryan, Front tracking for hyperbolic systems, Adv. Appl. Math. 2 (1981) 91–119.
[15] J. Glimm, D. Marchesin, O. McBryan, Stable and unstable fluid interface surfaces in petroleum engineering, Technical Report preprint, Rockefeller University, 1980.
[16] J.W. Grove, Applications of front tracking to the simulation of shock refractions and unstable mixing, J. Appl. Numer. Math. 14 (1994) 213–237.
[17] J.W. Grove, R. Menikoff, The anomalous reflection of a shock wave at a material interface, J. Fluid Mech. 219 (1990) 313–336.
[18] C.W. Hirt, A.A. Amsden, J.L. Cook, An arbitrary Lagrangian–Eulerian computing method for all flow speeds, J. Comput. Phys. 14 (1974) 227–253, Reprinted in 135 (1997) 203–216.
[19] X.-L. Li, Study of three dimensional Rayleigh–Taylor instability in compressible fluids through level set method and parallel computation, Phys. Fluids A 5 (1993) 1904–1913.
[20] X.F. Liu, E. George, W. Bo, J. Glimm, Turbulent mixing with physical mass diffusion, Phys. Rev. E 73 (2006) 056301-1–056301-8.
[21] L.G. Margolin, Introduction to an arbitrary Lagrangian–Eulerian computing method for all flow speeds, J. Comput. Phys. 135 (1997) 198–202.
[22] D.H. Sharp, An overview of Rayleigh–Taylor instability, Physica D 12 (1984) 3–18.
[23] V.S. Smeeton, D.L. Youngs, Experimental investigation of turbulent mixing by Rayleigh–Taylor instability (part 3), AWE Report Number 0 35/87, 1987.